Ab initio electronic conductivity of Fe-bearing post-perovskite

Yihang Peng [1,*] Yupei Zhang [2] Shuai Zhang [3] Chenxing Luo [1,4] Donghao Zheng [1]
Nelson Naveas [5] Xifan Wu [2] and Jie Deng [1,†]

[1]*Department of Geosciences, Princeton University, Princeton, New Jersey 08540, USA*
[2]*Department of Physics, Temple University, Philadelphia, Pennsylvania 19122, USA*
[3]*Laboratory for Laser Energetics, University of Rochester, Rochester, New York 14623, USA*
[4]*Department of Applied Physics and Applied Mathematics, Columbia University, New York, New York 10027, USA*
[5]*Departamento de Física Aplicada and Instituto Universitario de Ciencia de Materiales "Nicolás Cabrera" (INC), Universidad Autónoma de Madrid, Campus de Cantoblanco, Madrid, Spain*

(Received 7 January 2026; revised 4 August 2026; accepted 7 October 2026; published 23 October 2026)

The electrical conductivity of high-pressure silicates profoundly influences the interior dynamics of rocky planets. Employing the Kubo-Greenwood formalism, we perform *ab initio* calculations of electronic conductivity in Fe-bearing post-perovskite under super-Earth mantle conditions, up to 4000 K and 500 GPa. Electronic structures are obtained via many-body perturbation theory, incorporating dynamical screening and correlations among localized Fe-3*d* orbitals. In contrast to (Fe,Mg)O, for which metallization has been reported at comparable conditions, our results indicate that post-perovskite with Earth-like Fe contents is unlikely to metallize in super-Earth mantles via band-gap closure, yielding negligible low-frequency conductivity. Thus band conduction is negligible under the conditions examined. Small-polaron hopping is a plausible explanation for the larger measured total conductivity, but testing this hypothesis requires explicit calculations beyond the present band-conduction treatment.

DOI: 10.1103/zm8r-2bww

I. INTRODUCTION

Understanding the dynamics and evolution of planets requires detailed knowledge of the transport properties of planet-forming materials. Electrical conductivity is a fundamental transport property that governs how planets respond to electromagnetic processes, whether generated internally by a planetary dynamo [1–3] or externally through star-planet magnetic interactions [4,5]. Recent studies suggest that silicate liquid [6] and (Fe,Mg)O [7–9] may become metallized due to the closure of band gap under Earth's lowermost mantle conditions. However, the electrical conductivity of the dominant mantle mineral at corresponding and higher pressures ($\gtrsim$130 GPa [10]), (Mg,Fe)SiO_3 post-perovskite (pPv), remains poorly understood. Since pPv is one of the most abundant phases in super-Earths (i.e., rocky exoplanets with masses ranging from 1 to 10 Earth masses) [11], a comprehensive understanding of its conductivity is not only important for constraining the structure of Earth's deep mantle, but also essential for modeling the interior dynamics and potential habitability of super-Earths.

Accurately determining the electrical conductivity under the extreme conditions where pPv is stable remains experimentally challenging. In this context, theoretical calculations play an indispensable role in addressing this issue. However, first-principles methods encounter significant challenges in modeling the electronic conductivity of Fe-bearing silicates. These difficulties stem from localized Fe-3*d* electrons, which conventional Kohn-Sham density functional theory (DFT) fails to capture adequately. Furthermore, the accuracy of such calculations is compromised by severe self-interaction errors and the absence of derivative discontinuities inherent in local and semilocal exchange-correlation functionals [12]. Consequently, these limitations substantially undermine the predictive capability of standard DFT for describing the electronic structure and conductivity of Fe-bearing post-perovskite under the extreme conditions prevalent in planetary mantles. Although the DFT + U method offers a straightforward and computationally efficient correction for localized 3*d* electrons in perovskites [13–15], it remains a static, localized mean-field approximation that retains significant self-interaction errors. Furthermore, the efficacy of this semiempirical approach is highly sensitive to the Hubbard U parameter, which varies with crystal structure, valence, and spin state [16–18]. On the other hand, hybrid DFT approaches [19,20] mitigate self-interaction errors and the lack of derivative discontinuities by incorporating a fraction of nonlocal exact exchange. Overall, hybrid DFT provides a more accurate description of transition metal-bearing materials, with improvements comparable to those from DFT + U in many aspects, despite not treating correlated *d* electrons in the same localized manner [21–23]. However, both the DFT + U and hybrid functional methods neglect dynamical screening effects, leading to notable discrepancies between calculated and experimental spectra [24–26]. The *GW* approximation, an electronic structure method within many-body perturbation theory, incorporates dynamical screening effects while significantly mitigating self-interaction errors. This

*Contact author: yhpeng@princeton.edu
†Contact author: jie.deng@princeton.edu

 ©2026 American Physical Society

framework computes accurate quasiparticle (QP) energies, making it a powerful and widely used tool for predicting electronic structure in various materials in weakly to moderately correlated systems [24–28]. However, this method has rarely been applied to geophysically relevant materials under extreme conditions. The compositional complexity of planet-forming materials and the finite-size effects inherent to conductivity calculations necessitate large systems [6]; achieving accurate high-temperature conductivities further requires statistical averaging over many molecular dynamics (MD) snapshots [29]. These constraints render one-shot G_0W_0 the only practical option, but the sensitivity of its results to the mean-field starting point demands careful selection of the input wave functions [30].

In this study, we explore the electronic conductivity of pPv by combining multiple advanced theories including DFT + U, hybrid functionals, and many-body G_0W_0 approximation, using finite-temperature *ab initio* MD simulations and the Kubo-Greenwood (KG) formula (Sec. II). We find that ferrous iron at dodecahedral sites in pPv remains in the high-spin state up to 500 GPa (Sec. A in Supplemental Material [31]). We establish a protocol to determine the appropriate mean-field starting point for G_0W_0 on transition-metal-bearing materials (Sec. B in Supplemental Material [31]) and develop a practical workflow for electronic conductivity calculations at the *GW* level (Sec. II). Our results show that electronic conduction plays only a minor role in pPv, marking an important step toward resolving the electrical conductivity in planetary deep interiors.

II. METHODS

A. GGA + U

GGA + U calculations were performed with QUANTUM ESPRESSO (QE) [32,33] code in the PBEsol approximation [34]. We utilized the projector-augmented wave (PAW) method with PAW datasets from the PSLIBRARY [35]. The valence electronic configurations are $3s^23p^63d^64s^2$, $2s^22p^63s^2$, $3s^23p^2$, and $2s^22p^4$ for Fe, Mg, Si, and O, respectively. We chose an energy cutoff of 80 Ry for electronic wave functions and 500 Ry for spin-charge density and potentials. The convergence threshold of all self-consistent field calculations was 1×10^{-6} Ry. The Hubbard correction [36] using the simplified formulation of Ref. [37] was applied to Fe-*3d* states with orthogonalized atomic orbitals. The Hubbard parameter U was either set to fixed values of 2 eV and 3 eV or self-consistently computed based on density-functional perturbation theory [38] using the HP [39] code implemented in QE following the approach described in previous studies on iron oxides [40–42]. The convergence threshold for the response function was 1×10^{-6} Ry along with a q-point mesh of $2 \times 2 \times 2$. The self-consistent calculations of the Hubbard U parameter (U_{sc}) were performed through an iterative procedure, involving structural optimization followed by recalculation of the Hubbard parameters for each newly relaxed crystal structure [43,44]. The U_{sc} values were iterated until the difference between two successive iterations was smaller than 0.01 eV, ensuring self-consistency. The converged U_{sc} values under different spin states and pressure conditions are reported in Table S2 [31]. The 20-atom unit cell of *Cmcm* $MgSiO_3$ pPv with one Mg^{2+} substituted by Fe^{2+} at a dodecahedral (A) site was used for the band structure calculations, while a $2 \times 1 \times 1$ supercell with one Mg^{2+} substituted by Fe^{2+} was used for all other static calculations. The Brillouin zone of the 20-atom unit cell, 40-atom supercell, and 160-atom supercell (Sec. II D) were sampled by $10 \times 3 \times 4$, $5 \times 3 \times 4$, and $2 \times 3 \times 2$ Monkhorst-Pack meshes, respectively. Structure optimizations were performed by relaxing atom positions with convergence thresholds of 0.005 eV/Å for the atomic force, 0.5 kbar for the pressure, and 1×10^{-6} Ry for the total energy. Phonon calculations were performed using the finite-displacement method with the PHONOPY [45] code and GGA + U_{sc} forces calculated from QE. The vibrational contributions to the free energy were calculated using the quasiharmonic approximation [46] implemented in the QHA [47] code.

B. Hybrid functionals

Ab initio calculations using the HSE06 hybrid functional [19,20] were performed using the PAW dataset with a plane-wave energy cutoff of 800 eV as implemented in the Vienna *ab initio* simulation package (VASP) [48]. The valence electronic configurations are consistent with GGA + U calculations. The HSE06 functional is a screened implementation of the PBE0 functional. The exchange-correlation energy of PBE0 is given by

$$E_{xc}^{PBE0} = aE_x^{HF} + (1-a)E_x^{PBE} + E_c^{PBE}, \quad (1)$$

where the exchange energy contains both Hartree-Fock (HF) (E_x^{HF}) and PBE [49] (E_x^{PBE}) exchange terms, whereas the correlation energy is from the PBE functional. The HSE06 functional partitions the exchange term into short-range and long-range components using a screening parameter optimized to balance computational efficiency and accuracy. The parameter a denotes the HF exchange mixing coefficient, i.e., the fraction of HF exchange. The value of a is 0.25 in standard PBE0 and HSE06 functionals derived from perturbation theory [50]. However, it is suggested that the optimal a value that reproduces the experimental data is actually system-dependent [51,52]. We therefore use standard HSE06 with $a = 0.25$ as the primary hybrid reference and $a = 0.30$ as a modest sensitivity test. Both choices yield gaps and conductivities close to the many-body *GW* results, with $a = 0.30$ slightly closer for the configuration examined. The $8 \times 2 \times 3$, $3 \times 2 \times 3$, and $1 \times 1 \times 1$ k-point grids were used for the 20-atom unit cell, 40-atom supercell, and 160-atom supercell, respectively, to reduce the computational cost. To ensure a direct comparison of electronic structure results obtained from different methods, the HSE calculations are directly performed on the configurations obtained from GGA + U_{sc} structure optimizations and MD simulations.

C. *GW* approximation

The one-shot G_0W_0 calculation for the QP energy from many-body perturbation theory was performed with the BERKELEYGW package [53,54] and QE, starting from both GGA and GGA + U wave functions, for the 160-atom MD

snapshots described in Sec. II D. We utilize the multiple-projector norm-conserving pseudopotentials generated by the Optimized Norm-Conserving Vanderbilt Pseudopotential package [55] with consistent valence electronic configurations. A single Γ point in the Brillouin zone was used to maintain a reasonable computational cost. The static inverse dielectric matrix is constructed within the random phase approximation (RPA) and the Hybertsen-Louie generalized plasmon-pole (HL-GPP) model is used to extend the dielectric response to nonzero frequencies. We employ a screened cutoff of 10 Ry and 10 000 bands to ensure convergence of the QP gap at the G_0W_0 level.

D. Electronic conductivity

The electronic density of states and electronic conductivity were calculated from ionic trajectories obtained by *ab initio* MD simulations using the GGA + U_{sc} functional. *Ab initio* MD simulations were performed by VASP under the canonical ensemble with the Nosé-Hoover thermostat [56], sampling the Brillouin zone at the Γ point with energy cutoffs of 500 eV and an energy tolerance of 10^{-4} eV. Finite temperature effects on the energy were considered using the Mermin functional with the Fermi-Dirac smearing [57,58]. The initial configurations for the MD simulations were generated by substituting 12.5 mol.% Mg with Fe in the 4 × 1 × 2 supercell of *Cmcm* $MgSiO_3$ pPv with 160 atoms, corresponding to an iron content similar to the Earth's mantle. The spatial distribution of Fe atoms was determined using the special quasirandom structure method implemented in the Alloy-Theoretic Automated Toolkit [59,60], which minimizes an objective function for each supercell to homogenize the local atomic environment. For each pressure and temperature condition, we extracted 10 snapshots from the equilibrated MD trajectory of at least 3 picoseconds in length. The minimum interval between snapshots used for the KG calculations was 200 fs. For each condition, we report the mean over these 10 snapshots; error bars denote one standard deviation across the snapshots.

At 200 GPa and 3000 K, we evaluated normalized temporal autocorrelation functions along the GGA + U_{sc} trajectory for the spin-combined and spin-resolved band gaps, the valence- and conduction-band-edge separations from the common Fermi level in both spin channels, the potential energy per atom, and the pressure (Fig. S6 [31]). All correlations decay to small fluctuations about zero well before 200 fs and their absolute values at 200 fs do not exceed 0.04. Thus the minimum 200-fs interval between KG snapshots is well beyond the observed correlation decay and is sufficient to treat the snapshots as statistically independent.

The electronic conductivity σ of each snapshot was calculated using the Kubo-Greenwood (KG) formula [61,62] as implemented in the KGEC [63] code for QE and kgoptics [64] code for VASP:

$$\sigma(\omega) = \frac{2\pi e^2\hbar^2}{3m_e^2 V\omega}\sum_{\alpha=1}^{3}\sum_{m,m'}(f(\epsilon_{m'}) - f(\epsilon_m)) \times |\langle m|\nabla_\alpha|m'\rangle|^2\,\delta(\epsilon_m - \epsilon_{m'} - \hbar\omega), \quad (2)$$

where ω is the frequency of the electric current; $\hbar$ is the reduced Planck constant; δ is the Dirac δ function; e and m_e are the electron charge and mass; the α sum runs over the three spatial directions; m and m' denote the Kohn-Sham (KS) wave functions with corresponding eigenvalues ϵ_m, $\epsilon_{m'}$ and associated Fermi-Dirac occupation numbers $f(\epsilon_m)$ and $f(\epsilon_{m'})$. This approach has been applied for various planet-forming materials under extreme conditions [6,9,29,65,66]. The δ function in Eq. (2) is approximated by a Gaussian with a broadening parameter Δ of 0.5 eV following Ref. [29] and the effect of Δ on the dc conductivity results (Fig. S3 [31]) is comparable with the statistical uncertainty of the conductivity calculated from different MD snapshots (Fig. S4 [31]). Since Eq. (2) becomes unphysical when $\hbar\omega < \Delta$, the direct-current (dc) conductivity σ_{dc} is obtained by linearly extrapolating to zero frequency. Notably, as the only open-source implementation of KG calculation compatible with QE, KGEC does not support the postprocessing of spin-polarized DFT calculations [63]. We therefore modified the original implementation to enable conductivity calculations for spin-polarized systems by adding a sum over spin states in Eq. (2). The finite-size effect on the electrical conductivity is evaluated by conducting MD simulations and KG conductivity calculations on supercells of different sizes using the GGA + U_{sc} functional. We find that a supercell containing 160 atoms used in this study provides sufficiently converged results (Fig. S4 [31]).

In the G_0W_0 approximation used in this study, we apply state-resolved corrections to the KS eigenvalues while keeping the KS eigenfunctions unchanged (i.e., a diagonal self-energy in the KS basis). Accordingly, in our KG conductivity calculations, we evaluate the velocity matrix elements $\langle m|\nabla_\alpha|m'\rangle$ with the starting-point wave functions (e.g., from DFT or DFT + U), while using the QP energies and corresponding Fermi-Dirac occupation numbers at the target temperature. Our tests show that, once the band energies are fixed by the QP corrections, replacing the KS wave functions by those from different functionals produces no appreciable change in the dc conductivity (Fig. S5 [31]). This insensitivity suggests that, for the systems studied, the dc conductivity is primarily governed by the energy spectrum rather than modest variations in the wave functions, thereby justifying the use of starting-point matrix elements combined with G_0W_0-corrected energies.

III. ELECTRONIC STRUCTURE

A. Finite-temperature density of states

Accurately describing the electronic structure of pPv is a crucial prerequisite for obtaining reliable conductivity. Figures 1 and 2 present the total density of states (DOS) and projected density of states (PDOS) for $(Mg_{28}Fe_4)Si_{32}O_{96}$ pPv at 200 GPa and 4000 K, evaluated on the same molecular-dynamics snapshot with several electronic-structure levels: standard GGA, GGA + U (with $U = 2$ eV, $U = 3$ eV, and $U_{sc} = 5.26$ eV), HSE06 with Hartree-Fock (HF) exchange fraction $a = 0.25$ and 0.30, and one-shot G_0W_0 starting from GGA and from GGA + U. The corresponding spin-combined band gaps are listed in Table S1 [31].

Standard GGA produces a spurious metallic solution with finite DOS at the Fermi level (E_F) (Fig. 1), mainly contributed by Fe-3d states (Fig. 2), consistent with overdelocalization from self-interaction error similar to FeO [16]. Introducing

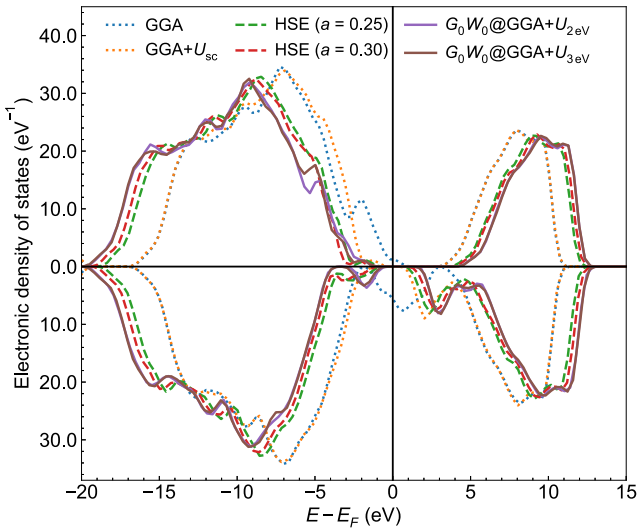


FIG. 1. Total electronic density of states of a molecular dynamics snapshot of $(Mg_{28}Fe_4)Si_{32}O_{96}$ pPv in high-spin state at 200 GPa and 4000 K obtained from different methods. The vertical black line represents the Fermi level (E_F). The upper and lower halves of the DOS plot correspond to the majority and minority spin states, respectively.

a self-consistently computed Hubbard U parameter (GGA + U_{sc}), nonlocal exchange (HSE), or dynamical screening effects (GW) systematically shifts the majority-spin Fe-3d states to lower energy and, in the minority-spin channel, splits the Fe-3d manifold into $d_{x^2-y^2}$ states at the valence band and other 3d states (d_{xy}, d_{xz}, d_{yz}, and d_{z^2}) at the conduction band, thereby opening a well-defined gap around E_F. The on-site Hubbard U correction primarily reorganizes Fe-3d states but maintains similar O-2p states compared to GGA, causing similar energies for O-2p and Fe-3d states and thus strong Fe–O hybridization at the valence band. By contrast, HSE and GW significantly shift the O-2p manifold away from the Fe-3d edges by reducing the energy of O-2p valence states, weakening p-d hybridization, and nudging the system toward a more Mott-Hubbard-like regime [67]. A similar functional dependence of the valence band character has been documented for olivine phosphates $LiMPO_4$ (M = Fe, Mn, Co, Ni): the application of Hubbard U often pushes the transition-metal 3d manifold below the O-2p states, yielding an O-2p-dominated valence band maximum (VBM), whereas HSE06, by placing O-2p states at higher binding energy, restores a transition-metal-derived VBM required by the experimentally inferred structural stability during delithiation [22,23]. By analogy, we regard the HSE and GW electronic structures for Fe-bearing pPv as a more reliable description than GGA + U_{sc}. Moreover, the two approaches—which both go beyond local Hubbard corrections by incorporating nonlocal exchange or dynamical screening—yield highly consistent DOS.

Relative to the standard HSE06 ($a = 0.25$), increasing HF exchange to 30% slightly enlarges both the Fe-3d splitting and the O-2p separation, in line with established trends for transition-metal oxides under PBE0/Fock-0.5-type mixing [21], producing a larger gap. To avoid inheriting an arbitrary parameter into the G_0W_0 results, we explicitly scanned GGA + U starting points to identify a range over which the GW DOS is weakly dependent on the input U. For U = 0–3 eV, the DOS of G_0W_0@GGA + U is essentially invariant. However, GGA + U itself with $U_{sc} = 5.26$ eV has already yielded a lower valence energy compared to G_0W_0@GGA + $U_{0\text{–}3\ eV}$. Since G_0W_0 further shifts the valence energy downward, a potential overcorrection of the $d_{x^2-y^2}$ states by G_0W_0@GGA + U_{sc} is observed (Fig. S2 [31]). In addition, since the starting wave function with band energies similar to the GW QP energies is considered better for the G_0W_0 method [26,68], we regard G_0W_0@GGA + $U_{2\text{–}3\ eV}$ as our most reliable QP reference and propose a similar starting-point sensitivity analysis as a general protocol for future G_0W_0 studies of transition-metal-bearing phases (see Sec. B in Supplemental Material [31] for details).

The characteristics of the DOS computed from configurations generated by MD simulations have direct implications for Kubo-Greenwood transport predictions. First, they demonstrate that thermal disorder at 4000 K does not restore metallicity once self-interaction is controlled: all beyond-GGA levels examined (GGA + U_{sc}, HSE, GW) retain a clear band gap on the MD snapshot and suggest low intraband conductivity. Second, by widening the O-2p separation and reducing p-d hybridization at the band edges, HSE and GW results show clear Mott-Hubbard character distinct from the mixed Mott-Hubbard/charge-transfer character obtained by GGA + U_{sc}, suggesting a reduced σ_{dc}.

B. Band structure and charge density of Fe-bearing post-perovskite

Figure 3 presents spin-resolved band structures of HS $(Mg_3Fe)Si_4O_{12}$ pPv at 200 GPa computed with GGA, GGA + U_{sc}, and standard HSE06 with $a = 0.25$. Across all functionals, the five bands closest to the Fermi level (E_F) carry dominant Fe-3d character, indicating that low-energy excitations are controlled by the Fe manifold and its hybridization with O-2p states (see also Fig. 2). In the majority channel [Figs. 3(a)–3(c)], all functionals yield a wide gap (≳5.2 eV from valence-band maximum to conduction-band minimum). In the minority channel [Figs. 3(d)–3(f)], standard GGA produces a metallic solution with Fe-3d bands crossing E_F. Introducing on-site correlation via GGA + U_{sc} splits the minority d manifold by shifting four d bands upward and one downward, opening a gap of ∼3 eV. HSE06 yields a very similar ordering and a slightly larger separation of Fe-3d bands compared to GGA + U_{sc}, which reflects similarly reduced self-interaction, but additionally shifts other bands: non-Fe states in the deeper valence and conduction regions move to lower and higher energies relative to GGA, respectively. By contrast, GGA + U_{sc} shows almost identical band structure with GGA except for Fe-3d states.

Figure 4 presents charge-density differences on the (001) plane of $(Mg_7Fe)Si_8O_{24}$ pPv intersecting the Mg and Fe sites, computed as $\rho_{GGA+U_{sc}} - \rho_{GGA}$ [Fig. 4(a)] and $\rho_{HSE06} - \rho_{GGA}$ [Fig. 4(b)]. Around Fe, both maps exhibit a four-lobe motif aligned with the x and y directions, i.e., the characteristic footprint of a $d_{x^2-y^2}$ orbital on this crystallographic cut. This anisotropy is expected because the majority-spin Fe-3d manifold is fully occupied (thus largely isotropic in its

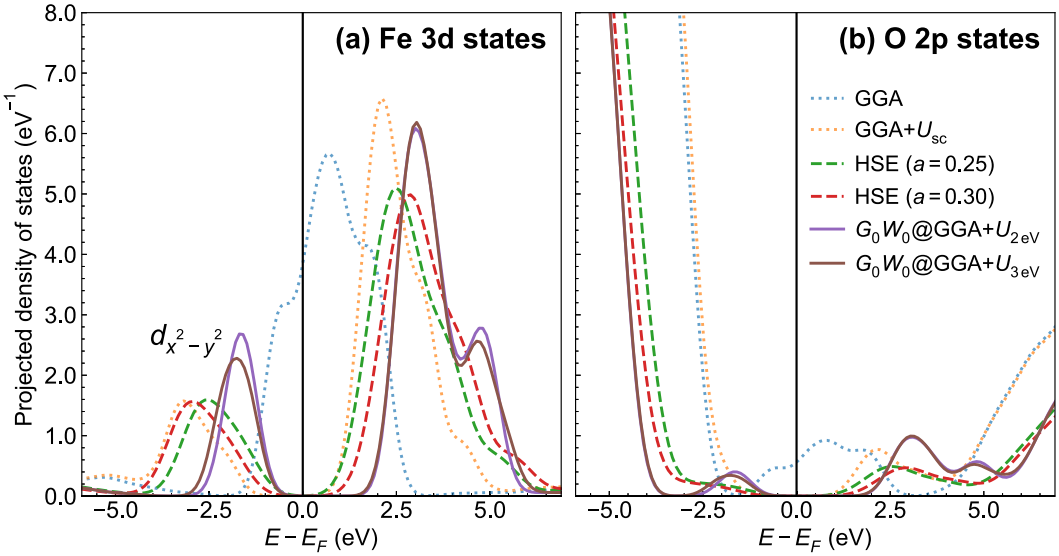


FIG. 2. Projected density of states (PDOS) for Fe-3d states (a) and O-2p states (b) in the same system as Fig. 1 obtained from different methods. Only the minority spin channel is shown. The vertical black lines represent the Fermi level (E_F).

net contribution) whereas, in the minority channel, only the lowest-energy $d_{x^2-y^2}$ state is occupied and contributes to the charge density, preserving its in-plane anisotropy. This finding is consistent with previous DFT + U_{sc} results [69].

The charge-density difference caused by the Hubbard U correction is highly localized: only Fe and the first-shell O ligands display noticeable changes, while more distant O and Mg sites are nearly unaffected [Fig. 4(a)]. By

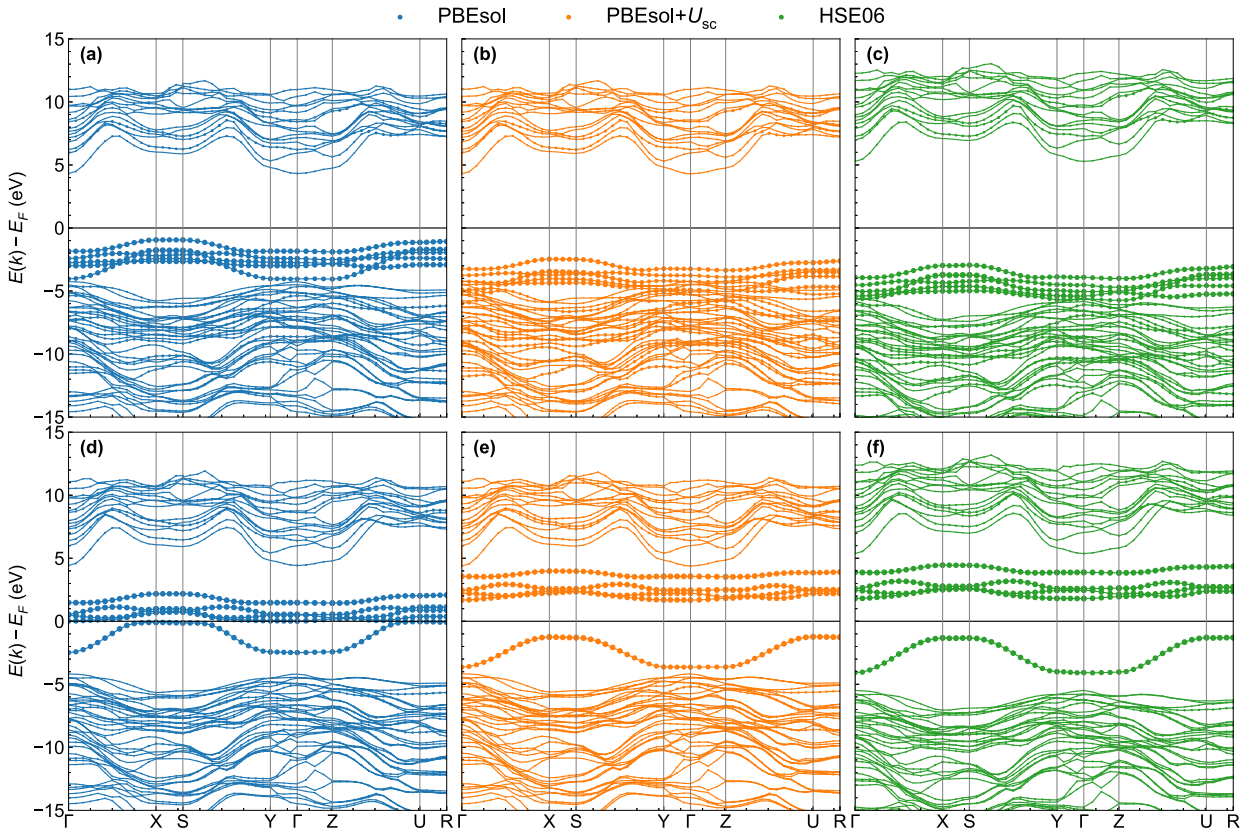


FIG. 3. Electronic band structure of $(Mg_3Fe)Si_4O_{12}$ pPv in high-spin state at 200 GPa computed with GGA (a), (d), GGA + U_{sc} (b), (e), and HSE06 (c), (f) functionals. The symbol size encodes the weight of Fe-3d states. (a)–(c) Majority spin; (d)–(f) minority spin. Because the calculation of the band structure requires using the pPv unit cell, introducing a single Fe atom results in an iron concentration that is twice that of the other systems reported in this study.

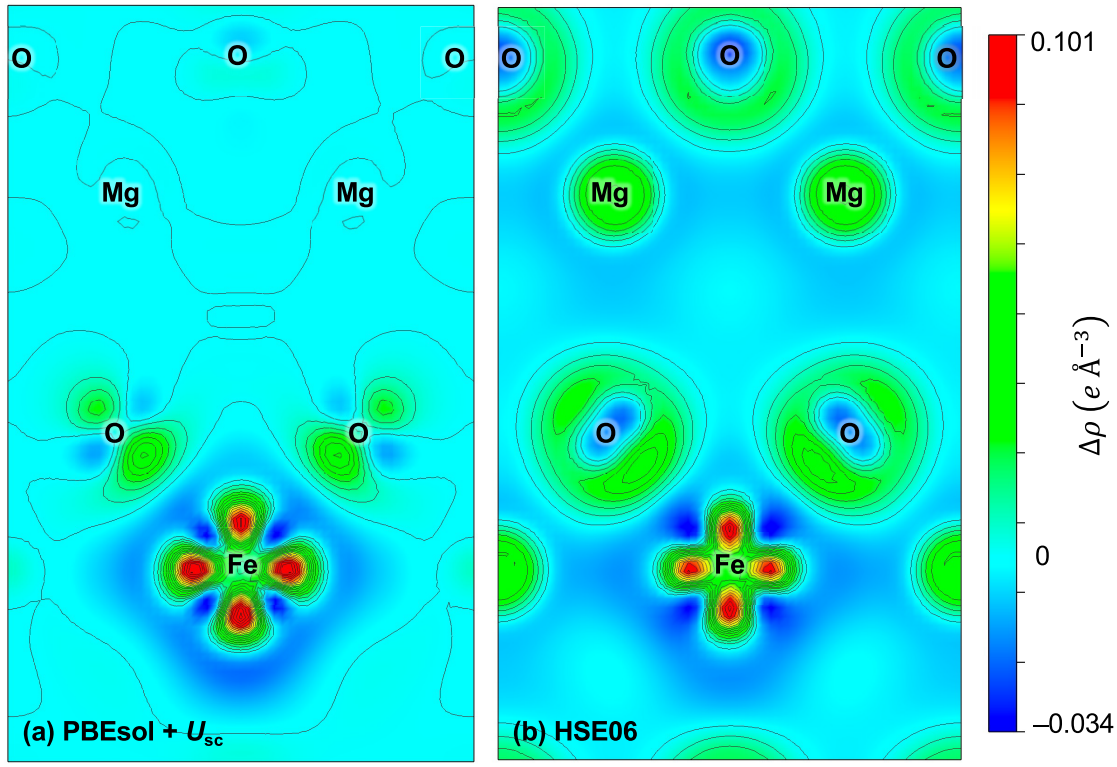


FIG. 4. Contour plots of the charge density (ρ) difference between different functionals on the (001) plane of $(Mg_7Fe)Si_8O_{24}$ pPv in high-spin state at 200 GPa. Red, yellow, and green indicate an accumulation of charge relative to GGA; blue indicates depletion. (a) $\rho_{\text{GGA}+U_{\text{sc}}} - \rho_{\text{GGA}}$; (b) $\rho_{\text{HSE06}} - \rho_{\text{GGA}}$.

correcting self-interaction on Fe-3d manifolds and generating a more localized Fe-centered pattern, Hubbard U also slightly reduces spurious Fe–O p–d hybridization in GGA and induces a compensating, oxygen-centered rebonding, shown as the reduced contribution of O-2p states to the DOS at E_F [Fig. 2(b)]. HSE06 produces a similar Fe-centered pattern but with a lattice-wide response, i.e., all Mg and O atoms show charge accumulation in the near-valence region. This nonlocal redistribution reflects the short-range exact-exchange component of HSE06, which reduces self-interaction for all valence states, compacts cation charge, and pushes O-2p bands away from the Fe-3d manifold (deepening the O-2p valence and raising O-2p contributions in the conduction band; see Fig. 3 and Fig. 2). A clear trend is observed from GGA to GGA + U and further to hybrid functionals, where the first-shell O ligands of Fe exhibit increasingly ionic character, aligning with earlier studies on hematite (α-Fe_2O_3) [30].

This real-space charge redistribution reinforces the interpretation drawn from the band structure. First, the tightening of Fe-3d charge and reduced p admixture at the band edges imply smaller conductivity under GGA + U_{sc} and HSE06. Second, the contrast between the highly local response under GGA + U_{sc} and the system-wide redistribution under HSE06 clarifies why HSE06 yields a larger gap and stronger suppression of low-energy conductivity: the hybrid functional does not simply localize Fe-3d electrons; it repartitions charge across the entire lattice, systematically reducing both self-interaction and the p–d hybridization that would enhance near-edge transitions. Together, the HSE reciprocal- and real-space response and the finite-temperature HSE–G_0W_0 DOS agreement increase confidence in the robustness and physical plausibility of both beyond-GGA descriptions relative to GGA + U_{sc}.

IV. ELECTRONIC CONDUCTIVITY

We evaluated the direct-current (dc) conductivity (σ_{dc}) of the same system using the KG formula Eq. (2), considering only the interband term because all levels of theory except standard GGA show a band gap (Table S1 [31]). To resolve how specific bands contribute to the conductivity, we decomposed the KG conductivity into individual contributions from band-pair transitions:

$$\sigma_{m,m'}(\omega) = \frac{2\pi e^2\hbar^2}{3m_e^2 V\omega}\sum_{\alpha=1}^{3}(f(\epsilon_{m'}) - f(\epsilon_m)) \times |\langle m|\nabla_\alpha|m'\rangle|^2\,\delta(\epsilon_m - \epsilon_{m'} - \hbar\omega). \quad (3)$$

The conductivity contributions are plotted in Fig. 5(a) on a common abscissa with the total DOS.

A pronounced spin asymmetry is observed [Fig. 5(a) and Fig. 3]. In the majority-spin channel, all methods beyond standard GGA yield a wide gap, rendering this channel largely inert for low-energy electronic transport with small contribution to σ_{dc}. However, since the two spin channels do not act as independent reservoirs and share a single chemical potential E_F, the majority-spin DOS is not symmetric with respect to E_F, causing thermally activated partial occupations

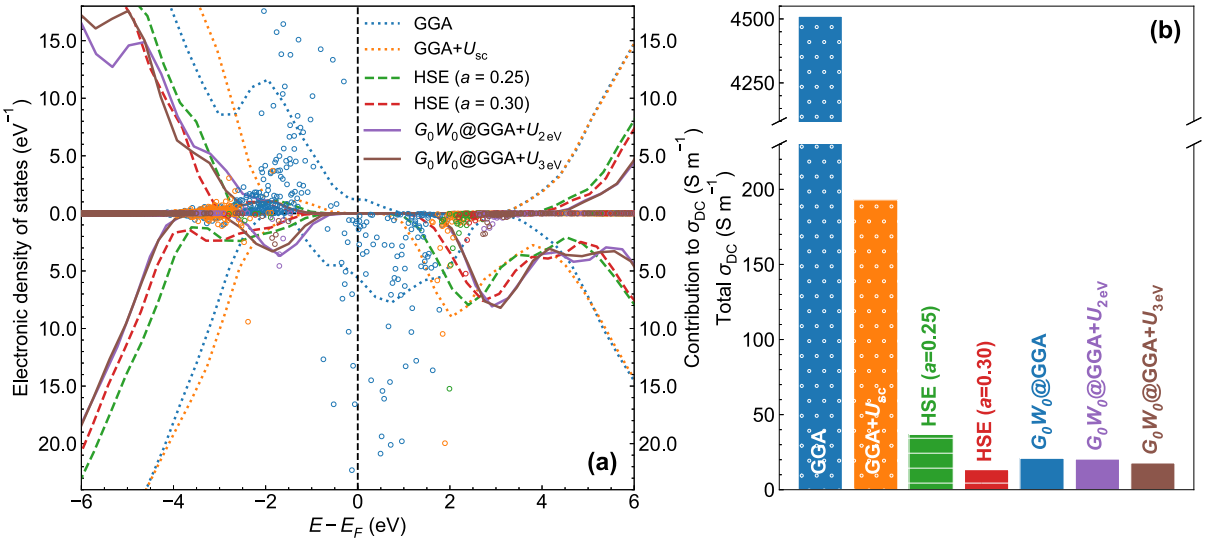


FIG. 5. (a) Decomposition of the Kubo-Greenwood dc conductivity of the same system as Fig. 1 obtained from different methods. Each electronic transition is shown by a data point (at the average energy of the initial and final bands) that gives the contribution of that transition to the dc conductivity. The density of states in Fig. 1 is also shown for comparison. The upward and downward directions of the plot represent the majority and minority spin states, respectively. (b) Total Kubo-Greenwood dc conductivity obtained from different methods, calculated as the summation of data points in (a).

near the valence band edge and a minor yet non-negligible contribution to σ_{dc} from the majority-spin channel, especially for GGA + U_{sc}.

For GGA, the spurious metallicity produces an extensive manifold of partially filled states at E_F, leading to many large contributions [many exceeding the y-axis ranges of Fig. 5(a)] and an overestimated total σ_{dc} of $\sim 4.5 \times 10^3$ S m^{-1}. Introducing a self-consistent Hubbard correction (GGA + U_{sc}) opens a gap and reduces σ_{dc} substantially; nevertheless, at the high temperature of 4000 K, the partial occupations at band edges still contribute to σ_{dc}. After applying U_{sc}, the Fe $d_{x^2-y^2}$ states become nearly degenerate with O-2p states that are weakly affected by Hubbard U at the valence band of the minority spin channel (Figs. 3 and 2). The resulting strong $p-d$ hybridization imparts a mixed Mott-Hubbard/charge-transfer character: both Fe-centered and ligand-centered holes appear and a combination of $d \to d$, $p \to d$, and $p \to p$ transitions produces a total σ_{dc} of $\sim$200 S m^{-1}.

Hybrid DFT and the *GW* approximation further reshape the pPv DOS and thus its electronic conductivity. The strongly reduced $p-d$ hybridization relative to GGA + U_{sc} confines thermally activated partial occupancies mainly to Fe-3d states, causing σ_{dc} to drop below $\sim$40 S m^{-1}. The four minority-spin $d_{x^2-y^2}$ states associated with the four Fe atoms form the valence band; thermally assisted transitions among these four states almost entirely control the valence-band contribution to the conductivity. Above E_F, the conduction band is dominated by the remaining 16 Fe-3d states, with only a small admixture of O-2p character arising from residual Fe-O hybridization; together these states govern the conduction-band contribution. HSE and *GW* place the two Fe-3d-dominated DOS peaks at slightly different energies: in HSE they are systematically lower in energy than in *GW* and thus HSE yields a larger conductivity contribution from the conduction band than from the valence band, whereas the opposite holds for *GW*. However, the resulting total conductivities remain comparable. The sharper band edges and deeper gap in the *GW* DOS further deplete the near-edge electronic transport relative to HSE, pushing σ_{dc} down to $<$20 S m^{-1}. Both $a = 0.25$ and 0.30 give conductivities close to G_0W_0; increasing a modestly enlarges the gap and lowers σ_{dc}, giving slightly closer agreement for this benchmark. By contrast, within a range of U values for the G_0W_0@GGA + U (U = 0–3 eV), the band-edge QP spectrum and σ_{dc} show no significant change, indicating desirable starting-point robustness at the *GW* level [Fig. 5(b)]. Using a GGA + U starting point with a larger U value leads to potential overcorrection by G_0W_0 (Sec. B in Supplemental Material [31]), but this would only increase the band gap and reduce σ_{dc}, which does not affect our conclusions. Overall, σ_{dc} obtained from different levels of theory decreases systematically following GGA $\gg$ GGA + U_{sc} > HSE (a = 0.25) $\gtrsim$ G_0W_0@GGA + U $\gtrsim$ HSE (a = 0.30). The progression reflects a systematic reduction of low-energy electronic transport as self-interaction is removed and dynamical screening is included.

V. ELECTRICAL CONDUCTIVITY IN PLANETARY MANTLES

Electrical conductivity in Fe-bearing mantle silicates is commonly attributed to small polaron conduction, involving hopping of charged polarons between Fe^{2+} and Fe^{3+} sites [71–73]. In contrast to small polaron conduction characterized by localized charge transport, band conduction involves delocalized electrons thermally excited into extended electronic states. The KG treatment used here describes this band contribution but does not represent the coupled electron-lattice hopping of a localized small polaron. The band conduction mechanism was proposed to become

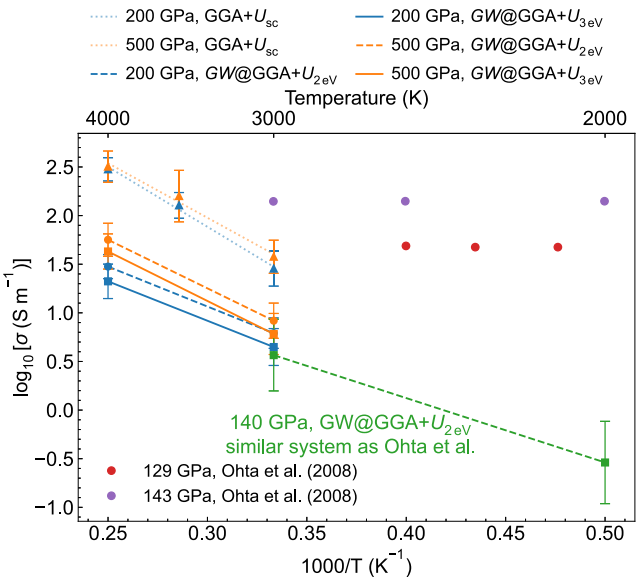


FIG. 6. Kubo-Greenwood dc conductivity of $(Mg_{28}Fe_4)Si_{32}O_{96}$ pPv (blue and orange) and $(Mg_{28}Fe_4)(Si_{31}Al)O_{96}$ pPv (green) in high-spin state under different pressure and temperature conditions. The error bars denote one standard deviation over 10 independent MD snapshots and quantify only snapshot-to-snapshot scatter; they exclude systematic uncertainty from the G_0W_0 quasiparticle gap, its starting-point dependence, finite size, and spectral broadening. The input-U and velocity-matrix sensitivities (Sec. B in Supplemental Material [31] and Fig. S5 [31]), finite-size effect (Fig. S4 [31]), and broadening parameter (Fig. S3 [31]) were tested separately, with the latter two evaluated at the GGA + U_{sc} level. These tests indicate numerical convergence or negligible sensitivity over the examined ranges; a semiquantitative gap-sensitivity estimate is given in the text. The experimental bulk conductivity of $(Mg_{0.89}Fe_{0.11})SiO_3$ pPv with $Fe^{3+}/\Sigma Fe = 0.13 \pm 0.10$ is shown for comparison without error bars because conductivity uncertainties were not reported [70].

dominant in (Mg,Fe)O and overtake small polaron conduction at temperatures above ∼2000 K [9]. To evaluate whether a similar crossover occurs in Fe-bearing pPv, we calculated GW-level σ_{dc} over a range of pressures and temperatures and compared them with experimental measurements under the Earth's core-mantle boundary conditions [70]. The means over 10 independent MD snapshots are shown in Fig. 6.

The structure we have discussed contains only ferrous iron occupying the dodecahedral (A) site. Nevertheless, in natural systems and experimental samples, ferric iron can be incorporated into mantle silicates via charge-coupled substitutions [74], with potential impacts on electronic structure and transport. For example, in the only available conductivity experiment on Fe-bearing pPv to date, the $(Mg_{0.89}Fe_{0.11})SiO_3$ sample had $Fe^{3+}/\Sigma Fe = 0.13 \pm 0.10$ [70]; in Al,Fe-bearing pPv, $Fe^{3+}/\Sigma Fe$ has been reported to exceed 50%, commonly attributed to $Fe^{3+}-Al^{3+}$ coupled substitution [75,76]. To facilitate a direct comparison with the experiment, we built a $(Mg_{28}Fe_4)(Si_{31}Al)O_{96}$ pPv supercell that approximates the sample's total Fe content and $Fe^{3+}/\Sigma Fe$ as closely as practicable. The Fe^{3+} is introduced via $Fe^{3+}-Al^{3+}$ coupled substitution to obtain $Fe^{3+}/\Sigma Fe = 0.25$ (about twice the experimental fraction owing to supercell size constraints). Since the Fe^{3+} still occupies the A site, the HS state remains energetically favorable up to 200 GPa [69]. Using G_0W_0@GGA + U, we evaluated its conductivity considering HS Fe at 140 GPa. Our results suggest that, under comparable temperature–pressure–composition conditions, the electronic conductivity of Fe-bearing pPv is much smaller than the experimentally measured total conductivity (Fig. 6). At 3000 K, the $(Mg_{28}Fe_4)(Si_{31}Al)O_{96}$ pPv yields ∼3.6 S m^{-1} at 140 GPa, which is close to and slightly lower than the value for $(Mg_{28}Fe_4)Si_{32}O_{96}$ pPv at 200 GPa, indicating that the presence of ferric iron does not substantially enhance electronic conduction. Ferric substitution at the level considered here does not collapse the gap nor increase $p-d$ hybridization within the GW framework.

We further examined whether a plausible G_0W_0 gap error could alter this comparison. As an illustrative test, we use a 0.5-eV downward gap shift, comparable to the 0.51-eV mean absolute error reported for the oxide subset of a 66-solid G_0W_0 benchmark [77]. Within the nondegenerate intrinsic-semiconductor approximation, $\sigma \propto \exp[-E_g/(2k_BT)]$ [78] gives a factor of about 2.6 at 3000 K. Although systematic uncertainties may shift the absolute conductivity, this stress test raises our value only from approximately 3.6 to 10 S m^{-1}, which is still more than an order of magnitude below the approximately 140 S m^{-1} measured at 143 GPa [70], indicating that band conduction contributes only a minor fraction of the total conductivity.

Due to the limited ionic diffusivity [79], the ionic conductivity in pPv is likely negligible. Therefore, under Earth's core-mantle boundary conditions, small-polaron hopping is the plausible dominant conduction mechanism, but its contribution cannot be quantified from the present band-conduction calculation. Ohta *et al.* measured total dc conductivity by resistance in a laser-heated diamond-anvil cell [70]. Their sample was dominated by pPv but contained minor perovskite, only the heated portion transformed, and the recovered pPv had $Fe^{3+}/\Sigma Fe = 0.13 \pm 0.10$ with uncontrolled oxygen fugacity. These phase, redox, and temperature heterogeneities, together with the absence of a reported conductivity uncertainty, preclude a precise partition of the measured total among transport mechanisms.

The pressure range in which pPv can stably exist within super-Earth mantles may extend up to 500 GPa [80,81]. For $(Mg_{0.875}Fe_{0.125})SiO_3$ pPv at 200–500 GPa and 3000–4000 K, σ_{dc} computed by both GGA + U_{sc} and G_0W_0@GGA + U exhibits weak pressure dependence and a clear thermal activation, with Arrhenius fits yielding activation enthalpies of 1.5–2 eV; however, GGA + U_{sc} systematically overestimates the conductivity by nearly an order of magnitude (Fig. 6). By contrast, the pPv conductivity measured by Ohta *et al.* is nearly temperature independent over approximately 2000–2500 K [70]. This qualitative mismatch is less sensitive to absolute normalization and indicates that the experiment likely probes transport physics absent from our band-conduction calculation, i.e., small polaron hopping. Even at 500 GPa and 4000 K—conditions corresponding to the core-mantle boundary of a 4-Earth-mass super-Earth with an Earth-like potential temperature—the electronic conductivity predicted by G_0W_0@GGA + U does not exceed 60 S m^{-1}.

We find that pPv with Earth-like iron content is unlikely to metallize in super-Earth mantles via band closure, so its band conduction remains negligible under the conditions examined. In contrast, iron-rich (Mg,Fe)O and FeO have reported metallization under Earth's lower mantle conditions [7,8]. Our GW-level results show that such metallization is not universal among Fe-bearing mantle phases: the dominant silicate phase pPv retains a robust gap, emphasizing strong mineralogical control on deep-mantle conductivity. However, early planetary evolution may involve extremely high interior temperatures and partial melting due to accretionary heating (e.g., Refs. [82,83]). Additionally, exoplanetary mantles may have diverse chemical compositions [84], potentially hosting significantly more Fe-rich silicates. Whether metallization occurs in pPv under these conditions requires further investigation and a full assessment of the electrical conductivity of Fe-bearing pPv will require explicit polaron hopping models beyond the band-to-band KG treatment.

VI. CONCLUSIONS

Where evaluated, all electronic-structure methods that control the self-interaction error retain a band gap in Fe-bearing pPv and the G_0W_0 calculations retain it throughout the scanned pressure-temperature range. Under comparable core–mantle-boundary conditions, the resulting band conductivity is negligible relative to the measured total conductivity; identifying the missing contribution, including the hypothesis of small-polaron hopping, requires a treatment beyond the present KG calculation.

Finally, this study underscores a methodological point: KG-based conductivity predictions are only as accurate as the underlying electronic structure and care must be taken to employ *ab initio* techniques that faithfully capture the intrinsic electronic properties of the target materials.

ACKNOWLEDGMENTS

We thank R. Car for useful discussion. This work was funded by the National Science Foundation under Grant No. EAR-2242946 to J.D. The work by Y.Z. and X.W. was supported by Seven Research, LLC. The work by S.Z. was supported by the Department of Energy (National Nuclear Security Administration), University of Rochester, National Inertial Confinement Program, under Award No. DE-NA0004144. The authors are pleased to acknowledge that the work reported in this paper was substantially performed using Princeton University's Research Computing resources. This research used resources of the National Energy Research Scientific Computing Center, a DOE Office of Science User Facility supported by the Office of Science of the U.S. Department of Energy under Contract No. DE-AC02-05CH11231 using NERSC Award No. BES-ERCAP0035544. This work used Anvil supercomputer at Purdue University through allocations EES250058 and EES250049 from the Advanced Cyberinfrastructure Coordination Ecosystem: Services & Support (ACCESS) program, which is supported by U.S. National Science Foundation (Grants No. 2138259, No. 2138286, No. 2138307, No. 2137603, and No. 2138296).

DATA AVAILABILITY

The data that support the findings of this article are publicly available in the Open Science Framework [85].

[1] R. J. Banks, Geomagnetic variations and the electrical conductivity of the upper mantle, Geophys. J. Int. **17**, 457 (1969).

[2] B. A. Buffett, Constraints on magnetic energy and mantle conductivity from the forced nutations of the Earth, J. Geophys. Res.: Solid Earth **97**, 19581 (1992).

[3] R. Vilim, S. Stanley, and L. Elkins-Tanton, The effect of lower mantle metallization on magnetic field generation in rocky exoplanets, Astrophys. J. Lett. **768**, L30 (2013).

[4] K. G. Kislyakova, L. Noack, C. P. Johnstone, V. V. Zaitsev, L. Fossati, H. Lammer, M. L. Khodachenko, P. Odert, and M. Güdel, Magma oceans and enhanced volcanism on TRAPPIST-1 planets due to induction heating, Nat. Astron. **1**, 878 (2017).

[5] Y. Peng, K. Kislyakova, D. Zheng, Z. Zhang, and J. Deng, Induction heating in super-Earths: A thermochemical perspective, Astrophys. J. Lett. **993**, L56 (2025).

[6] L. Stixrude, R. Scipioni, and M. P. Desjarlais, A silicate dynamo in the early Earth, Nat. Commun. **11**, 935 (2020).

[7] K. Ohta, R. E. Cohen, K. Hirose, K. Haule, K. Shimizu, and Y. Ohishi, Experimental and theoretical evidence for pressure-induced metallization in FeO with rocksalt-type structure, Phys. Rev. Lett. **108**, 026403 (2012).

[8] K. Ohta, K. Fujino, Y. Kuwayama, T. Kondo, K. Shimizu, and Y. Ohishi, Highly conductive iron-rich (Mg,Fe)O magnesiowüstite and its stability in the Earth's lower mantle, J. Geophys. Res.: Solid Earth **119**, 4656 (2014).

[9] E. Holmström, L. Stixrude, R. Scipioni, and A.S. Foster, Electronic conductivity of solid and liquid (Mg,Fe)O computed from first principles, Earth Planet. Sci. Lett. **490**, 11 (2018).

[10] M. Murakami, K. Hirose, K. Kawamura, N. Sata, and Y. Ohishi, Post-perovskite phase transition in $MgSiO_3$, Science **304**, 855 (2004).

[11] F. W. Wagner, N. Tosi, F. Sohl, H. Rauer, and T. Spohn, Rocky super-Earth interiors: Structure and internal dynamics of CoRoT-7b and Kepler-10b, Astron. Astrophys. **541**, A103 (2012).

[12] A. J. Cohen, P. Mori-Sánchez, and W. Yang, Insights into current limitations of density functional theory, Science **321**, 792 (2008).

[13] M. Cococcioni, Accurate and efficient calculations on strongly correlated minerals with the LDA+U method: Review and perspectives, Rev. Mineral. Geochem. **71**, 147 (2010).

[14] H. Wang, L. He, H. Jiang, C. Steele, and X. Wu, Electronic origin of the spin-phonon coupling effect in transition-metal perovskites, Phys. Rev. B **96**, 075121 (2017).

[15] H. Wang, F. Tang, M. Stengel, H. Xiang, Q. An, T. Low, and X. Wu, Convert widespread paraelectric

perovskite to ferroelectrics, Phys. Rev. Lett. **128**, 197601 (2022).
[16] M. Cococcioni and S. de Gironcoli, Linear response approach to the calculation of the effective interaction parameters in the LDA + U method, Phys. Rev. B **71**, 035105 (2005).
[17] H. Hsu, K. Umemoto, Z. Wu, and R. M. Wentzcovitch, Spin-state crossover of iron in lower-mantle minerals: Results of DFT+U investigations, Rev. Mineral. Geochem. **71**, 169 (2010).
[18] A. Floris, I. Timrov, B. Himmetoglu, N. Marzari, S. de Gironcoli, and M. Cococcioni, Hubbard-corrected density functional perturbation theory with ultrasoft pseudopotentials, Phys. Rev. B **101**, 064305 (2020).
[19] J. Heyd, G. E. Scuseria, and M. Ernzerhof, Hybrid functionals based on a screened Coulomb potential, J. Chem. Phys. **118**, 8207 (2003).
[20] J. Paier, M. Marsman, K. Hummer, G. Kresse, I. C. Gerber, and J. G. Ángyán, Screened hybrid density functionals applied to solids, J. Chem. Phys. **124**, 154709 (2006).
[21] F. Tran, P. Blaha, K. Schwarz, and P. Novák, Hybrid exchange-correlation energy functionals for strongly correlated electrons: Applications to transition-metal monoxides, Phys. Rev. B **74**, 155108 (2006).
[22] M. D. Johannes, K. Hoang, J. L. Allen, and K. Gaskell, Hole polaron formation and migration in olivine phosphate materials, Phys. Rev. B **85**, 115106 (2012).
[23] Y. Zhang, J. A. Alarco, A. S. Best, G. A. Snook, P. C. Talbot, and J. Y. Nerkar, Re-evaluation of experimental measurements for the validation of electronic band structure calculations for $LiFePO_4$ and $FePO_4$, RSC Adv. **9**, 1134 (2019).
[24] C. Rödl, F. Fuchs, J. Furthmüller, and F. Bechstedt, Quasiparticle band structures of the antiferromagnetic transition-metal oxides MnO, FeO, CoO, and NiO, Phys. Rev. B **79**, 235114 (2009).
[25] Y. Nohara, S. Yamamoto, and T. Fujiwara, Electronic structure of perovskite-type transition metal oxides $LaMO_3$ (M = Ti ∼ Cu) by $U + GW$ approximation, Phys. Rev. B **79**, 195110 (2009).
[26] S. Lany, Band-structure calculations for the 3*d* transition metal oxides in *GW*, Phys. Rev. B **87**, 085112 (2013).
[27] S. V. Faleev, M. van Schilfgaarde, and T. Kotani, All-electron self-consistent *GW* approximation: Application to Si, MnO, and NiO, Phys. Rev. Lett. **93**, 126406 (2004).
[28] P. Rinke, A. Qteish, J. Neugebauer, C. Freysoldt, and M. Scheffler, Combining *GW* calculations with exact-exchange density-functional theory: An analysis of valence-band photoemission for compound semiconductors, New J. Phys. **7**, 126 (2005).
[29] M. Ghosh, S. X. Hu, E. Blackman, T.-A. Suer, and S. Zhang, Melting and transport properties of Al_2O_3 at extreme conditions, Phys. Rev. B **110**, 174107 (2024).
[30] P. Liao and E. A. Carter, Testing variations of the GW approximation on strongly correlated transition metal oxides: Hematite (α-Fe_2O_3) as a benchmark, Phys. Chem. Chem. Phys. **13**, 15189 (2011).
[31] See Supplemental Material at http://link.aps.org/supplemental/10.1103/zm8r-2bww for spin-state energetics, starting-point dependence of G_0W_0, band-gap and Hubbard-U tables, conductivity validation tests, and molecular-dynamics autocorrelation analysis, which includes Refs. [86–91].
[32] P. Giannozzi, S. Baroni, N. Bonini, M. Calandra, R. Car, C. Cavazzoni, D. Ceresoli, G. L. Chiarotti, M. Cococcioni, I. Dabo, A. Dal Corso, S. de Gironcoli, S. Fabris, G. Fratesi, R. Gebauer, U. Gerstmann, C. Gougoussis, A. Kokalj, M. Lazzeri, L. Martin-Samos, *et al.*, QUANTUM ESPRESSO: A modular and open-source software project for quantum simulations of materials, J. Phys.: Condens. Matter **21**, 395502 (2009).
[33] P. Giannozzi, O. Andreussi, T. Brumme, O. Bunau, M. Buongiorno Nardelli, M. Calandra, R. Car, C. Cavazzoni, D. Ceresoli, M. Cococcioni, N. Colonna, I. Carnimeo, A. Dal Corso, S. de Gironcoli, P. Delugas, R. A. DiStasio Jr, A. Ferretti, A. Floris, G. Fratesi, G. Fugallo, *et al.*, Advanced capabilities for materials modelling with QUANTUM ESPRESSO, J. Phys.: Condens. Matter **29**, 465901 (2017).
[34] J. P. Perdew, A. Ruzsinszky, G. I. Csonka, O. A. Vydrov, G. E. Scuseria, L. A. Constantin, X. L. Zhou, and K. Burke, Restoring the density-gradient expansion for exchange in solids and surfaces, Phys. Rev. Lett. **100**, 136406 (2008).
[35] A. Dal Corso, Pseudopotentials periodic table: From H to Pu, Comput. Mater. Sci. **95**, 337 (2014).
[36] V. I. Anisimov, J. Zaanen, and O. K. Andersen, Band theory and Mott insulators: Hubbard U instead of Stoner I, Phys. Rev. B **44**, 943 (1991).
[37] S. L. Dudarev, G. A. Botton, S. Y. Savrasov, C. J. Humphreys, and A. P. Sutton, Electron-energy-loss spectra and the structural stability of nickel oxide: An LSDA+U study, Phys. Rev. B **57**, 1505 (1998).
[38] I. Timrov, N. Marzari, and M. Cococcioni, Hubbard parameters from density-functional perturbation theory, Phys. Rev. B **98**, 085127 (2018).
[39] I. Timrov, N. Marzari, and M. Cococcioni, HP–A code for the calculation of Hubbard parameters using density-functional perturbation theory, Comput. Phys. Commun. **279**, 108455 (2022).
[40] N. Naveas, R. Pulido, C. Marini, J. Hernández-Montelongo, and M. M. Silván, First-principles calculations of hematite (α-Fe_2O_3) by self-consistent DFT+U+V, iScience **26**, 106033 (2023).
[41] N. Naveas, R. Pulido, C. Marini, P. Gargiani, J. Hernandez-Montelongo, I. Brito, and M. Manso-Silván, First-principles calculations of magnetite (Fe_3O_4) above the Verwey temperature by using self-consistent DFT + U + V, J. Chem. Theory Comput. **19**, 8610 (2023).
[42] N. Naveas, F. J. Fernández-Alonso, R. Pulido, R. J. Martin-Palma, J. Hernández-Montelongo, C. T. Sousa, and M. Manso-Silván, DFT + U + V approach to Fe_3O_4 (001): Insights into surface chemistry and Cu^{2+} adsorption, Results Phys. **70**, 108158 (2025).
[43] H. Hsu, P. Blaha, M. Cococcioni, and R. M. Wentzcovitch, Spin-state crossover and hyperfine interactions of ferric iron in $MgSiO_3$ perovskite, Phys. Rev. Lett. **106**, 118501 (2011).
[44] I. Timrov, N. Marzari, and M. Cococcioni, Self-consistent Hubbard parameters from density-functional perturbation theory in the ultrasoft and projector-augmented wave formulations, Phys. Rev. B **103**, 045141 (2021).
[45] A. Togo and I. Tanaka, First principles phonon calculations in materials science, Scr. Mater. **108**, 1 (2015).

[46] D. C. Wallace and H. Callen, Thermodynamics of crystals, Am. J. Phys. **40**, 1718 (1972).
[47] T. Qin, Q. Zhang, R. M. Wentzcovitch, and K. Umemoto, qha: A Python package for quasiharmonic free energy calculation for multi-configuration systems, Comput. Phys. Commun. **237**, 199 (2019).
[48] G. Kresse and J. Furthmüller, Efficient iterative schemes for *ab initio* total-energy calculations using a plane-wave basis set, Phys. Rev. B **54**, 11169 (1996).
[49] J. P. Perdew, K. Burke, and M. Ernzerhof, Generalized gradient approximation made simple, Phys. Rev. Lett. **77**, 3865 (1996).
[50] J. P. Perdew, M. Ernzerhof, and K. Burke, Rationale for mixing exact exchange with density functional approximations, J. Chem. Phys. **105**, 9982 (1996).
[51] J. Heyd and G. E. Scuseria, Efficient hybrid density functional calculations in solids: Assessment of the Heyd–Scuseria–Ernzerhof screened Coulomb hybrid functional, J. Chem. Phys. **121**, 1187 (2004).
[52] Y. Meng, X.-W. Liu, C.-F. Huo, W.-P. Guo, D.-B. Cao, Q. Peng, A. Dearden, X. Gonze, Y. Yang, J. Wang, H. Jiao, Y. Li, and X.-D. Wen, When density functional approximations meet iron oxides, J. Chem. Theory Comput. **12**, 5132 (2016).
[53] M. S. Hybertsen and S. G. Louie, Electron correlation in semiconductors and insulators: Band gaps and quasiparticle energies, Phys. Rev. B **34**, 5390 (1986).
[54] J. Deslippe, G. Samsonidze, D. A. Strubbe, M. Jain, M. L. Cohen, and S. G. Louie, BerkeleyGW: A massively parallel computer package for the calculation of the quasiparticle and optical properties of materials and nanostructures, Comput. Phys. Commun. **183**, 1269 (2012).
[55] D. R. Hamann, Optimized norm-conserving Vanderbilt pseudopotentials, Phys. Rev. B **88**, 085117 (2013).
[56] W. G. Hoover, Canonical dynamics: Equilibrium phase-space distributions, Phys. Rev. A **31**, 1695 (1985).
[57] N. D. Mermin, Thermal properties of the inhomogeneous electron gas, Phys. Rev. **137**, A1441 (1965).
[58] R. M. Wentzcovitch, J. L. Martins, and P. B. Allen, Energy versus free-energy conservation in first-principles molecular dynamics, Phys. Rev. B **45**, 11372 (1992).
[59] C. Jiang, C. Wolverton, J. Sofo, L.-Q. Chen, and Z.-K. Liu, First-principles study of binary bcc alloys using special quasirandom structures, Phys. Rev. B **69**, 214202 (2004).
[60] A. van de Walle, P. Tiwary, M. de Jong, D.L. Olmsted, M. Asta, A. Dick, D. Shin, Y. Wang, L.-Q. Chen, and Z.-K. Liu, Efficient stochastic generation of special quasirandom structures, Calphad **42**, 13 (2013).
[61] R. Kubo, Statistical-mechanical theory of irreversible processes. I. General theory and simple applications to magnetic and conduction problems, J. Phys. Soc. Jpn. **12**, 570 (1957).
[62] D. A. Greenwood, The Boltzmann equation in the theory of electrical conduction in metals, Proc. Phys. Soc. **71**, 585 (1958).
[63] L. Calderín, V. V. Karasiev, and S. B. Trickey, Kubo–Greenwood electrical conductivity formulation and implementation for projector augmented wave datasets, Comput. Phys. Commun. **221**, 118 (2017).
[64] M. P. Desjarlais, J. D. Kress, and L. A. Collins, Electrical conductivity for warm, dense aluminum plasmas and liquids, Phys. Rev. E **66**, 025401(R) (2002).
[65] R. Scipioni, L. Stixrude, and M. P. Desjarlais, Electrical conductivity of SiO_2 at extreme conditions and planetary dynamos, Proc. Natl. Acad. Sci. USA **114**, 9009 (2017).
[66] F. Soubiran and B. Militzer, Electrical conductivity and magnetic dynamos in magma oceans of super-Earths, Nat. Commun. **9**, 3883 (2018).
[67] A. Fujimori, T. Yoshida, K. Okazaki, T. Tsujioka, K. Kobayashi, T. Mizokawa, M. Onoda, T. Katsufuji, Y. Taguchi, and Y. Tokura, Electronic structure of Mott–Hubbard-type transition-metal oxides, J. Electron Spectrosc. Relat. Phenom. **117–118**, 277 (2001).
[68] F. Fuchs, J. Furthmüller, F. Bechstedt, M. Shishkin, and G. Kresse, Quasiparticle band structure based on a generalized Kohn-Sham scheme, Phys. Rev. B **76**, 115109 (2007).
[69] Y. G. Yu, H. Hsu, M. Cococcioni, and R. M. Wentzcovitch, Spin states and hyperfine interactions of iron incorporated in $MgSiO_3$ post-perovskite, Earth Planet. Sci. Lett. **331–332**, 1 (2012).
[70] K. Ohta, S. Onoda, K. Hirose, R. Sinmyo, K. Shimizu, N. Sata, Y. Ohishi, and A. Yasuhara, The electrical conductivity of post-perovskite in Earth's D″ layer, Science **320**, 89 (2008).
[71] T. Yoshino, Laboratory electrical conductivity measurement of mantle minerals, Surv. Geophys. **31**, 163 (2010).
[72] T. Yoshino and T. Katsura, Electrical conductivity of mantle minerals: Role of water in conductivity anomalies, Annu. Rev. Earth Planet Sci. **41**, 605 (2013).
[73] T. Yoshino, S. Kamada, C. C. Zhao, E. Ohtani, and N. Hirao, Electrical conductivity model of Al-bearing bridgmanite with implications for the electrical structure of the Earth's lower mantle, Earth Planet. Sci. Lett. **434**, 208 (2016).
[74] R. Huang, T. Boffa Ballaran, C. A. McCammon, N. Miyajima, and D. J. Frost, The effect of Fe-Al substitution on the crystal structure of $MgSiO_3$ bridgmanite, J. Geophys. Res.: Solid Earth **126**, e2021JB021936 (2021).
[75] R. Sinmyo, K. Hirose, H. St. C. O'Neill, and E. Okunishi, Ferric iron in Al-bearing post-perovskite, Geophys. Res. Lett. **33**, L12S13 (2006).
[76] R. Sinmyo, H. Ozawa, K. Hirose, A. Yasuhara, N. Endo, N. Sata, and Y. Ohishi, Ferric iron content in $(Mg,Fe)SiO_3$ perovskite and post-perovskite at deep lower mantle conditions, Am. Mineral. **93**, 1899 (2008).
[77] Á. Morales-García, R. Valero, and F. Illas, An empirical, yet practical way to predict the band gap in solids by using density functional band structure calculations, J. Phys. Chem. C **121**, 18862 (2017).
[78] A. Roy, R. Dey, T. Pramanik, A. Rai, R. Schalip, S. Majumder, S. Guchhait, and S. K. Banerjee, Structural and magnetic properties of molecular beam epitaxy grown chromium selenide thin films, Phys. Rev. Mater. **4**, 025001 (2020).
[79] M. W. Ammann, J. P. Brodholt, J. Wookey, and D. P. Dobson, First-principles constraints on diffusion in lower-mantle minerals and a weak D″ layer, Nature (London) **465**, 462 (2010).
[80] K. Umemoto, R. M. Wentzcovitch, S. Wu, M. Ji, C.-Z. Wang, and K.-M. Ho, Phase transitions in $MgSiO_3$ post-perovskite in super-Earth mantles, Earth Planet. Sci. Lett. **478**, 40 (2017).
[81] R. Dutta, S. J. Tracy, and R. E. Cohen, High-pressure order-disorder transition in Mg_2SiO_4: Implications for super-Earth mineralogy, Phys. Rev. B **107**, 184112 (2023).
[82] L. Stixrude, Melting in super-earths, Philos. Trans. R. Soc. A **372**, 20130076 (2014).

[83] A. Vazan, C. W. Ormel, L. Noack, and C. Dominik, Contribution of the core to the thermal evolution of sub-Neptunes, Astrophys. J. **869**, 163 (2018).

[84] P. Hatalova, J. P. Brodholt, R. Brasser, Y. Shan, and S. Werner, The compositional diversity of rocky exoplanets around K-dwarf stars, Astron. Astrophys. **694**, A303 (2025).

[85] Y. Peng and J. Deng, *Ab initio* electronic conductivity of Fe-bearing post-perovskite [Dataset], Open Science Framework, 2026, https://doi.org/10.17605/OSF.IO/JZNVQ.

[86] J. Badro, Spin transitions in mantle minerals, Annu. Rev. Earth Planet Sci. **42**, 231 (2014).

[87] H. Hsu, K. Umemoto, P. Blaha, and R. M. Wentzcovitch, Spin states and hyperfine interactions of iron in (Mg,Fe)SiO_3 perovskite under pressure, Earth Planet. Sci. Lett. **294**, 19 (2010).

[88] Y. Sun, M. Cococcioni, and R. M. Wentzcovitch, LDA + U_{sc} calculations of phase relations in FeO, Phys. Rev. Mater. **4**, 063605 (2020).

[89] E. Holmström and L. Stixrude, Spin crossover in ferropericlase from first-principles molecular dynamics, Phys. Rev. Lett. **114**, 117202 (2015).

[90] G. Grimvall, Spin disorder in paramagnetic fcc iron, Phys. Rev. B **39**, 12300 (1989).

[91] J. Deng, H. Niu, J. Hu, M. Chen, and L. Stixrude, Melting of $MgSiO_3$ determined by machine learning potentials, Phys. Rev. B **107**, 064103 (2023).